Corrosion Science 249 (2025) 112851

Contents lists available at ScienceDirect

Corrosion Science

journal homepage: www.elsevier.com/locate/corsci

Correlated chromium carbide dissociation and phase transformation in liquid lead-bismuth eutectic corroded T91 steel

Minyi Zhang [a,*], Guanze He [a], Robin Scales [a], Kay Song [b], Mark Lapington [b], Weiyue Zhou [c], Zhiyuan Ding [a], Michael P. Short [c], Paul A.J. Bagot [a], Michael P. Moody [a], Felix Hofmann [b,*]

[a] Department of Materials, University of Oxford, Oxford OX1 3PH, United Kingdom
[b] Department of Engineering, University of Oxford, Oxford OX1 3PJ, United Kingdom
[c] Department of Nuclear Science and Engineering, Massachusetts Institute of Technology, Cambridge, MA 02139, USA

ARTICLE INFO

Keywords:
Lead cooled fast reactor
F/M steels
Cr depletion
Carbides dissociation
Phase transformation

ABSTRACT

Gen IV nuclear reactors promise better safety, economic benefits and a potential path to reducing carbon emissions. The liquid lead-bismuth eutectic (LBE) cooled fast reactor is a key Gen IV reactor concept. This study investigates the corrosion of T91 steel, a candidate structural material for Gen IV reactors, exposed to liquid LBE. Specifically, we focus on the dissociation of Cr carbides and the overall Cr depletion adjacent to the corrosion interface. Our results suggest a correlation between Cr depletion and phase transformation in the steel, most likely ferritization. We have analysed the corrosion-induced changes from the micro- to atomic-scale by combining complementary characterisation techniques: SEM, EDX, (HR)EBSD, DAXM, (S)TEM, EELS, and APT. Based on these investigations, we propose a potential mechanism of Cr depletion, Cr carbides dissociation, and phase transformation in T91 induced by LBE exposure. These microstructural changes may alter the mechanical properties, and are thus of direct importance to reactor designs, safety, and lifetime estimation.

1. Introduction

T91 is one of the candidate structural steels for Gen IV fission reactors, concentrated solar power plants, and accelerator-driven subcritical system (ADS) nuclear reactors [1–3]. Lead alloys are being tested as coolants because of their higher safety and temperature limits [4]. However, regardless of the application, corrosion of structural materials in liquid metal at high temperatures remains a major concern. The cost of replacing corroded structural components, together with the possibility of lost revenue due to related unplanned shutdown of the plants, has the potential to severely impact the economic viability of these designs. Most importantly, the safe day-to-day operation of the plant is the ultimate consideration. Further study is needed to clarify the dominant corrosion mechanisms, thus enabling more accurate lifetime predictions for lead-exposed steels during service, and to further refine steel design to improve corrosion-resistance.

The operating temperature of current lead-bismuth eutectic (LBE) cooled reactor designs is limited to 450℃ to 500℃, with passivation (oxide layer at the surface) used as the main anti-corrosion method. However, above 550℃ passivation will no longer work for traditional steels, such as SS316 or T91, due to the phase transformation of iron oxide from Magnetite to Wüstite, which is is porous and thus cannot act as an effective corrosion barrier. This limits the use of passivation to protect steels [5,6]. Also, due to the difficulty of precisely controlling oxygen content in a reactor system, there could be local regions with lower oxygen content than desired, rendering the corrosion to be oxygen deficient. To raise the operational temperature of these systems, which is critical for increasing their thermal efficiency, we thus need to understand how the steels corrode under reducing conditions.

It has been previously reported that in an oxygen-deficient environment, physical dissolution of elements from the steel into the LBE is the primary mechanism driving corrosion [7,8]. The dealloying of steel during liquid metal corrosion under reducing conditions follows a different mechanism to molten-salt corrosion [7,9]. The corrosion of alloys in molten salt environments is governed by a combination of thermodynamically driven corrosion, salt impurity-induced corrosion, thermal gradient-driven corrosion, and galvanic corrosion resulting from electrochemical potential differences between dissimilar materials [10]. However, the element diffusion process in LBE is a much more physical process [7]. Moreover, elemental diffusion will be further

* Corresponding authors.
E-mail addresses: minyi.zhang@materials.ox.ac.uk (M. Zhang), felix.hofmann@eng.ox.ac.uk (F. Hofmann).

https://doi.org/10.1016/j.corsci.2025.112851
Received 31 December 2024; Received in revised form 15 February 2025; Accepted 6 March 2025
Available online 6 March 2025

exacerbated at higher temperatures. This restricts the range of operating temperatures, which in turn impedes the efficiency of LBE as an effective coolant and the resulting economic benefits. Thus, a better understanding of corrosion mechanisms is needed from many perspectives.

Steel corrosion in liquid metals occurs as elements, mainly Fe, Cr, and Ni, dissolve into the liquid phase at the steel/liquid-metal interface until saturation is reached. Since metal solubility decreases with temperature, non-uniform temperatures cause dissolved metals to move and re-deposit in cooler areas through convection (in a moving liquid) or diffusion (in a static melt) [11]. Austenitic and ferritic/martensitic (F/M) steels are the two main types of steel being considered as candidate cladding structural materials in these reactors. Austenitic steels contain higher amounts of Ni and Mn to stabilise the austenite phase, while Cr is added to increase hardness and high temperature corrosion resistance. However, a transformation of austenite to ferrite, known as ferritization, has been observed near the corrosion surface. Literature suggests that the preferential dissolution of Ni and Mn into LBE is the main driving force behind this phenomenon [12,13]. The tendency for ferritization increases with higher temperature and correlates to faster corrosion of the material [14]. Thus, the preferential leaching of alloying elements from the surface of the steel limits the use of austenitic steels at higher temperatures [13].

In contrast to the austenitic steels, F/M steels have relatively lower content of Ni and Cr. For F/M steel exposed to LBE, no obvious large area phase transformation is observed across different test temperatures [14]. From this perspective, the use of F/M steels potentially allows the reactor plants to operate at higher temperatures. However, other factors must also be considered, for example, liquid metal embrittlement and creep [15–17].

Previously, we have undertaken a systematic analysis of T91 steel samples corroded in static LBE under reducing environment, proposing a possible mechanism by which the corrosion proceeds [18]. We observed the disappearance of Cr-rich precipitates and an apparent phase change in the Cr-depleted region adjacent to the corrosion front. However, this was not investigated in detail, and we were unable to fully explain the dissociation of Cr precipitates and the observed phase changes at the corrosion-affected surface. Cr precipitates have a major influence on the material strength and crack susceptibility of F/M steels [19]. There have been limited previous studies in which the dissolution of Cr-rich precipitates was observed in F/M steels exposed to LBE corrosion [20]. The dissociation of Cr-rich precipitates has also been observed in other alloy systems when exposed to different environments: For example, Was and Allen reported $Cr_{23}C_6$ dissociation in Ni-Cr alloys, for helium-cooled reactors, following exposure to CO and CO_2 atmosphere [21]. They proposed a dissolution mechanism that acts above a critical temperature and was driven by decarburization of the alloy through the formation of CO, resulting in a region depleted of carbon near the corroded surface [22]. Was et al. also suggested that Cr depletion, caused by the preferential dissolution of Cr, is the driving force for the dissociation of Cr carbides in molten salt-cooled reactors [23]. Durham et al. observed Cr carbide dissociation in oxidised Fe-Cr-C alloys, explaining this phenomenon as the result of carbon diffusion to the alloy surface, undergoing oxidation to form carbon monoxide, and then diffusing through the scale, along nano-scale defects, presumably as carbon monoxide molecules [24]. They also reason that the carbide size will influence dissociation in austenitic steels, which have a lower diffusion rate, while this effect is small in F/M steels as these have a higher C diffusivity. There are few prior works in the literature [25,26] that consider LBE corrosion induced phase transformation in F/M steels.

In the present study, we investigate the mechanisms leading to Cr precipitate dissociation and phase transformation by characterising the surface microstructure of LBE-corroded T91 steel across a range of different length scales. Scanning electron microscopy (SEM) equipped with energy-dispersive X-ray spectroscopy (EDX) and electron backscatter diffraction (EBSD) detectors, and micro-beam Laue X-ray diffraction were used to study micro-scale material structure. Scanning transmission electron microscopy (STEM) equipped with EDX and electron energy loss spectroscopy (EELS) detectors provides nanoscale information. Atom probe tomography (APT) is used to provide complementary precise measurements of C contents in the matrix.

2. Methods

2.1. Materials

Ultra-pure (99.999 wt%) lead and bismuth were purchased from Surepure Chemetals, Inc. and mixed according to a eutectic composition of lead (44.5 *at* %) and bismuth (55.5 *at* %).

T91, a ferritic/martensitic (F/M) steel, were purchased from Edelstahl Witten-Krefeld GMBH in the quenched and tempered condition, having undergone heat treatment in accordance with the manufacturer's specifications [27]. The standard heat treatment for T91 involves normalizing at 1040–1080°C (1900–1975°F) followed by air cooling, then tempering at 730–800°C (1350–1470°F). This process ensures the desired mechanical properties, including a Brinell hardness range of approximately 190–248 HBW, making the alloy suitable for high-temperature structural applications. All the samples were cut from the same bar using wire electrical discharge machining (EDM) to dimensions of 25 mm x 25 mm x 3–4 mm. The composition from the alloy certificate is listed in Table 1.

2.2. Static corrosion tests

Samples were polished down to 50 nm alumina suspensions to produce a mirror finish on one side. The other side was ground with 120 grit SiC paper. Samples were then submerged in LBE for 70, 245, and 506 h at 715 °C. The oxygen level was between the equilibrium oxygen potential of Fe_3O_4 and $FeCr_2O_4$ at the testing temperature [28]. The actual oxygen potentials of the cover gases were below the detection limit of the sensors used. Consequently, the measured concentrations of hydrogen and water vapour were used to estimate the oxygen partial pressures and concentrations. The estimated value was below 1×10^{-26} atm (1.8×10^{-9} wt%) [29]. The oxygen weight percentages were calculated using the method described in [30]. A detailed description of the static corrosion experiments is provided elsewhere [31].

Samples were subsequently mounted in Bakelite with the cross-section (starting with corroded LBE and T91 interface at left and the T91 matrix at right side) facing outwards, with the LBE-exposed surfaces in contact with the Bakelite. Next, samples were ground with SiC grinding paper to 4000 grit, polished with diamond suspension to 1 μm, and then completed with colloidal silica polishing.

2.3. Characterization techniques

The morphology and microscale chemical composition of the cross-sections of the corroded samples were examined by scanning electron microscopy (SEM) using a Zeiss Merlin FEG-SEM equipped with a Bruker XFlash FlatQUAD 5060 F EDX detector and Bruker e-flash high-resolution EBSD detector. The working distance for EDX was 18 mm and electron beam voltage ranged from 5 kV to 20 kV [32]. Electron Backscatter Diffraction (EBSD) maps were obtained at a working distance of 18 mm and a sample tilt of 70°, with a beam voltage of 20 kV and 5–10 nA probe current.

Total geometrically necessary dislocation (GND) density maps, similar to those produced by Britton and Wilkinson using the high-resolution EBSD (HR-EBSD) approach [33], were generated from the EBSD data using custom MATLAB codes. Further details of the HR-EBSD methodology to obtain GND densities are provided elsewhere [34].

The crystal structure of different parts of the corroded sample was probed by X-ray micro-diffraction at the 34-ID-E beamline at the Advanced Photon Source (Argonne National Laboratory, IL, USA). The sample was mounted in 45° reflection geometry and 2D Laue diffraction

Table 1
Composition of T91 material according to the alloy certificate provided by the manufacturer (wt%).

Fe	Cr	Mo	Si	Mn	Ni	V	C	Nb	N	P	Al
89.0	8.76	0.93	0.34	0.50	0.30	0.20	0.09	0.07	0.05	0.02	0.01

patterns were collected on an area detector positioned above the sample. An incident polychromatic beam (7–30 keV) with a size of 185 x 360 nm^2 on the surface was used. A line scan was taken along the polished sample cross-section. Depth resolution was achieved using the Differential Aperture X-ray Microscopy (DAXM) technique [35,36]. Briefly, a platinum wire is scanned along the surface of the sample, cutting through the diffracted beam. By triangulating using the positions of the incident beam, detector and wire, a profile of the intensity reaching each pixel on the detector as a function of depth in the sample (along the beam path) can be reconstructed. This allows depth-resolved measurements of grain orientation on a 2D slice at a 45° angle into the cross-section surface. Indexing of the diffraction patterns was performed using the LaueGo software package (J.Z. Tischler: tischler@anl.gov).

Two plan-view TEM samples were prepared using a Zeiss NVision 40 FIB-SEM system following the approach in [37]. One includes the LBE while the other is adjacent to the first, but closer to the unaffected matrix. The TEM samples were lifted out onto a Cu grid, then thinned to less than 100 nm thickness using 30 kV Ga ions with beam currents ranging from 700 pA to 40 pA. The final step used 2 kV, 200 pA Ga ion polishing to remove surface defects induced by the 30 kV Ga ions. STEM images were recorded using a Jeol ARM 200 F cold-FEG TEM operating at 200 kV, fitted with a 100 mm^2 Centurion EDX detector and Gatan GIF Quantum 965 ER, allowing for EDX and EELS map acquisition in regions of interest. The step size for the EDX and EELS maps was 5 nm.

APT specimens were prepared using a dual-beam Zeiss Crossbeam 540 FIB-SEM. The samples were first trenched and then lifted out and attached to standard silicon micro tip coupons. Next, annular FIB milling was used to mill the samples into sharp needles with tip diameters < 100 nm. An acceleration voltage of 30 kV was used for FIB milling, followed by a final low-energy polishing step (2 kV, 200 pA) to remove FIB-induced surface damage. APT samples were analysed using a Cameca LEAP 5000XR atom probe. A laser energy of 50 pJ, stage temperature of 50 K, pulse frequency of 200 kHz, and detection rate of 0.5 were used for all measurements.

3. Results

3.1. Baseline of as-received T91

Electron microscopy results for as-received T91 are shown in Fig. 1. A high-magnification SEM micrograph is presented in Fig. 1(a) with precipitates visible along prior-austenite grain boundaries (GBs) and martensite lath boundaries. The compositions of these precipitates are analysed in detail below using TEM. Lower magnification EBSD and EDX results are shown in Fig. 1(b) and Fig. 1(c) to provide an overview of the microstructure across a larger area. The EBSD grain map in Fig. 1(b) shows the expected martensite lath structure within the as-received T91. Fig. 1(c) shows an EDX map for Cr. Cr is present in the matrix, in precipitates and at GBs. Neither Cr depletion nor precipitate dissociation are observed either at the sample surface or elsewhere.

3.2. Phase transformation and carbide dissociation observed in corroded samples

There is obvious phase change observed in 245 h corroded samples. Characterisations were done on this sample to illustrate the mechanism. Fig. 2 shows SEM-EBSD and SEM-EDX maps for T91 corroded in LBE for 245 h in a reducing environment. Fig. 2(a) is a larger scale map, while Fig. 2(b)-(e) show a close-up of the region at the surface where changes are observed, as marked with a yellow dashed rectangle in Fig. 2(a). In Fig. 2, the LBE penetrates T91 from the left side which is marked with an orange arrow in Fig. 2(d).

Fig. 2(a) and (b) show that the grain structure adjacent to the corroded region has transformed from martensite laths to more equiaxed grains with lower grain average misorientation. This suggests that a phase transformation has occurred in this region. Fig. 2(c) shows the geometry necessary dislocation (GND) density of the same area. The phase transformed grains on the left-hand side show much lower GND density compared to original martensite laths. Compared to both the as-received sample in Fig. 1(b) and the uncorroded sub-surface martensite lath structure on the right-hand side of Fig. 2(a), it is apparent that the grain morphology change near the left surface is triggered by LBE static corrosion rather than a direct result of surface effects or temperature influence. EDX analysis of the same area in Fig. 2(d) shows the Fe and Cr distributions. Fe is presented to give an approximate indication of the location of the T91 surface. From Fig. 2(d), we can observe that the Cr depletion region extends over 10 μm from the LBE-exposed surface. This is most likely due to the higher solubility and diffusion speed of Cr compared to Fe in LBE [38]. Furthermore, there is an apparent dissociation of Cr-rich precipitates that were formerly within this Cr depletion region. Referring to Fig. 1(c), it is reasonable to propose that the Cr depletion observed in Fig. 2(d) is caused by LBE corrosion. Changes in the content of other elements at the interface, such as Ni, Si, and V, are also observed, as shown in supplementary figure S1. However, as shown in Fig. 2, the changes in Cr content closely correlate with the phase transformation in the affected region, with Cr exhibiting higher concentrations in T91. In contrast, the other elements showed no clear correlation and were present in much lower amounts. This supports the primary role of Cr in the observed phase changes.

Next, 33 EDX line scans normal to the surface were acquired, distributed evenly across Fig. 2(d). The mean profiles determined for both Cr and Fe, superimposed on the SEM image showing grains, are

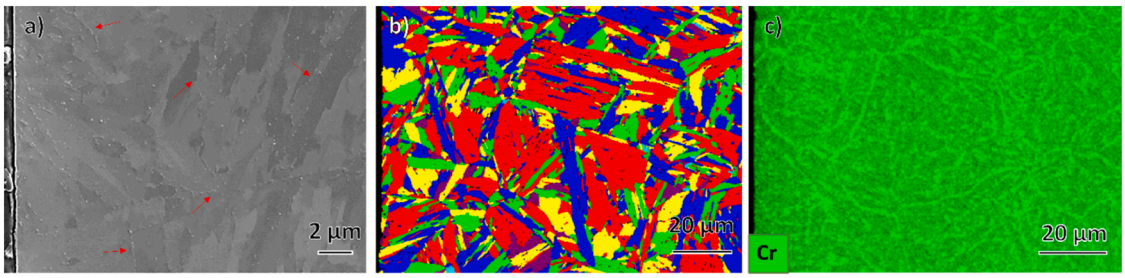

Fig. 1. Microstructure of the as-received T91 material. a) SEM map with red arrows highlighting some of the visible precipitates. b) EBSD-grain map showing the expected martensite lath structure. c) EDX map of Cr showing Cr presents in the matrix, precipitates and GBs.

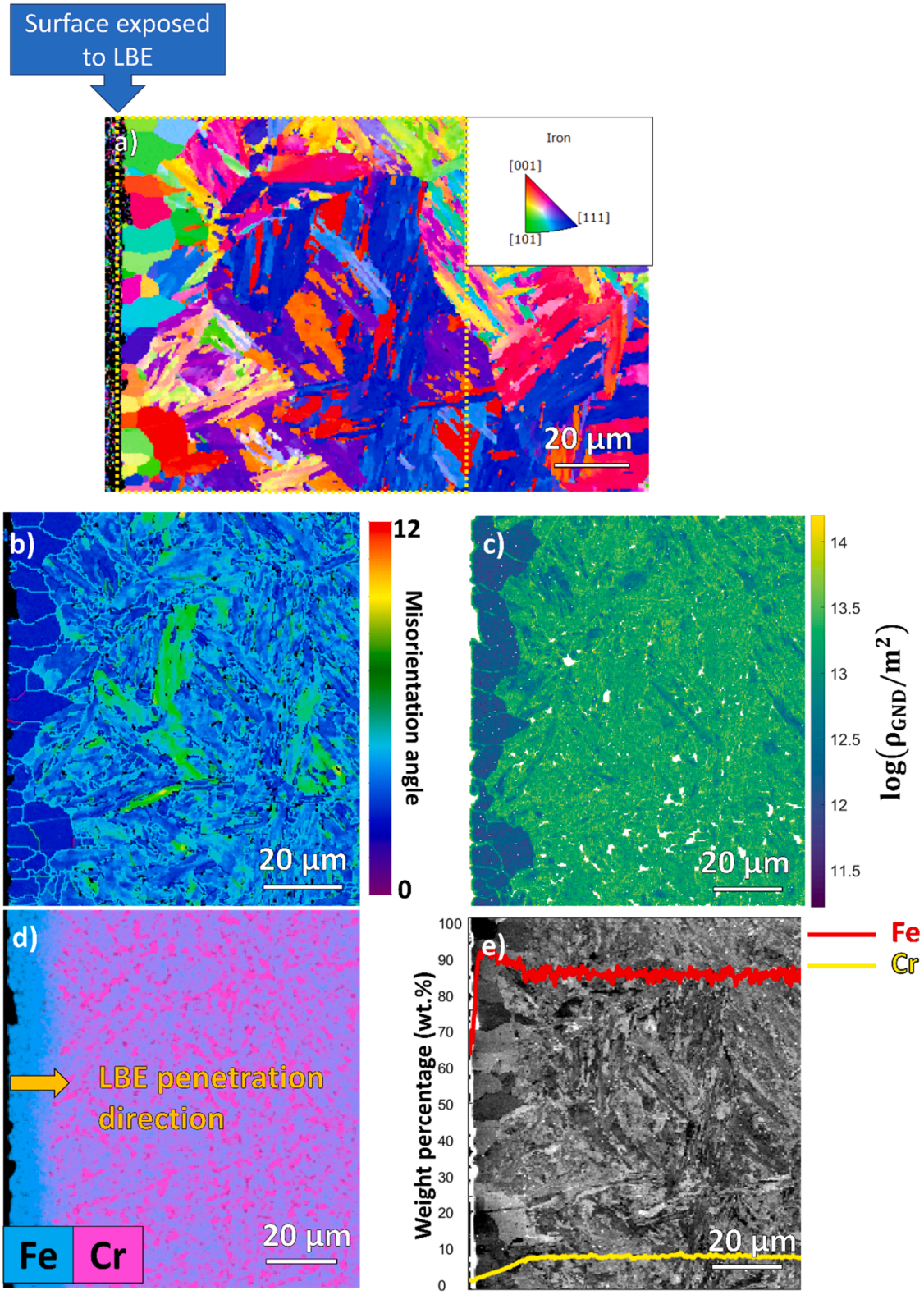

Fig. 2. Cross-section SEM-EBSD and EDX results for the sample exposed to LBE corrosion for 245 h at 715 °C. (a) EBSD IPFZ Map with the yellow dashed rectangle highlighting region for subsequent analysis in (b), (c), (d), & (e). (b) EBSD grain average misorientation map with scale bar. (c) GND density map. (d) EDX map showing Cr and Fe. (e) Overlay of EDX line-scan results from Fe (red) and Cr (yellow) on SEM grain map.

plotted Fig. 2(e). Fe and Cr are the main elements in T91 and are assumed to play the most prominent roles. Thus, these two elements are considered here. The results show that the proposed phase transformation region at the surface closely correlates with the volume within which Cr was depleted and where Cr-rich precipitates have dissociated. This would appear to suggest that the two phenomena are linked. Corroded samples corresponding to exposure times of 70 h and 506 h show similar grain morphology changes, as presented in supplementary

figure S2.

Several studies have reported an austenite-to-ferrite transformation at the surface of austenitic stainless steels that were exposed to liquid LBE at elevated temperatures (T > 450℃) [13,39]. Because of the dissolution of highly soluble austenite stabilizers (i.e., Ni and Mn) from austenite into the LBE, the material eventually transforms from face-centred cubic (fcc) austenite to body-centred cubic (bcc) ferrite. This change in crystal structure can be readily distinguished in the EBSD analysis map. However, in the present study, the crystal structure of the body-centred tetragonal martensite closely resembles the bcc ferrite, making them more challenging to distinguish. For our T91 material, the C content is 0.09 wt% which is relatively low and leads to a c/a ratio close to 1, making it difficult to differentiate martensite from ferrite using individual EBSD patterns [40]. Thus, X-ray diffraction, which offers higher angular resolution, is used as an additional method to determine the crystallography.

Differential Aperture X-ray Microscopy (DAXM) was used to determine the crystallography within a 2D slice oriented at 45° to the polished surface of the sample as illustrated in Fig. 3(a). The depth-resolved patterns were indexed assuming a ferritic crystal structure (a_0 = 0.287 nm). The indexed results are shown in Fig. 3(b), with the LBE-exposed surface on the left at x = 0, and the polished surface of the sample on the bottom at d = 0. The region within 15 μm of the LBE-exposed surface indexes to a ferritic structure to a much greater extent than the rest of the sample further away from the LBE-exposed surface. This suggests that this region has more ferritic character than the bulk.

Furthermore, there are significant qualitative differences in the diffraction patterns at different distances from the LBE-exposed surface as shown in Fig. 3(c) to (f). Close to the LBE-exposed surface (x = 2 μm), the diffraction peak appears very circular with high intensity, suggesting a low-strain crystal structure. This is characteristic of a recrystallised ferritic microstructure. Moving further away from the LBE-exposed surface, the shape of the diffraction peak becomes less symmetric and more 'smeared', which is an indication of increasing strain heterogeneity [41–44]. Far away from the LBE-exposed surface (x = 25 – 35 μm), the peaks have much lower scattering intensity, indicating smaller grain size. Diffraction patterns of several grains can be identified at once and usually with very small amounts of misorientation (~1°) between them. This is consistent with diffraction from a martensitic lath structure [45].

Alongside the EBSD measurements in Fig. 2(a), Fig. 2(b), and GND calculation in Fig. 2(c), we can conclude that while the bulk of the T91 sample remains martensitic, regions closer to the LBE-exposed surface adopt a ferritic character. The length scale over which the ferritic microstructure is observed with DAXM (~15 μm) agrees closely with the length scale of low GND grains in Fig. 2(b) and width of the Cr-depleted zone shown in Fig. 2(e).

3.3. *Influence of Cr depletion on phase transformation*

To further investigate the correlation between Cr depletion and phase transformation, we identified three distinct near-surface regions significantly differing in the level of Cr depletion (as shown in Fig. 4(a) and divided by black horizontal dashed lines) and acquired EDX and EBSD data from these regions. The results are presented in Fig. 4. The sample surface is marked with the yellow dashed line and the location of the scans in Fig. 4(b) and (c) is highlighted with a dark blue dashed rectangle in Fig. 4(a). Comparing the averaged EDX line scans (each region acquired over 10 line scans evenly spaced over the area) of the three regions shown in Fig. 4(a), it can be seen that the upper region has limited Cr depletion. Furthermore, the Cr-enriched precipitates in this

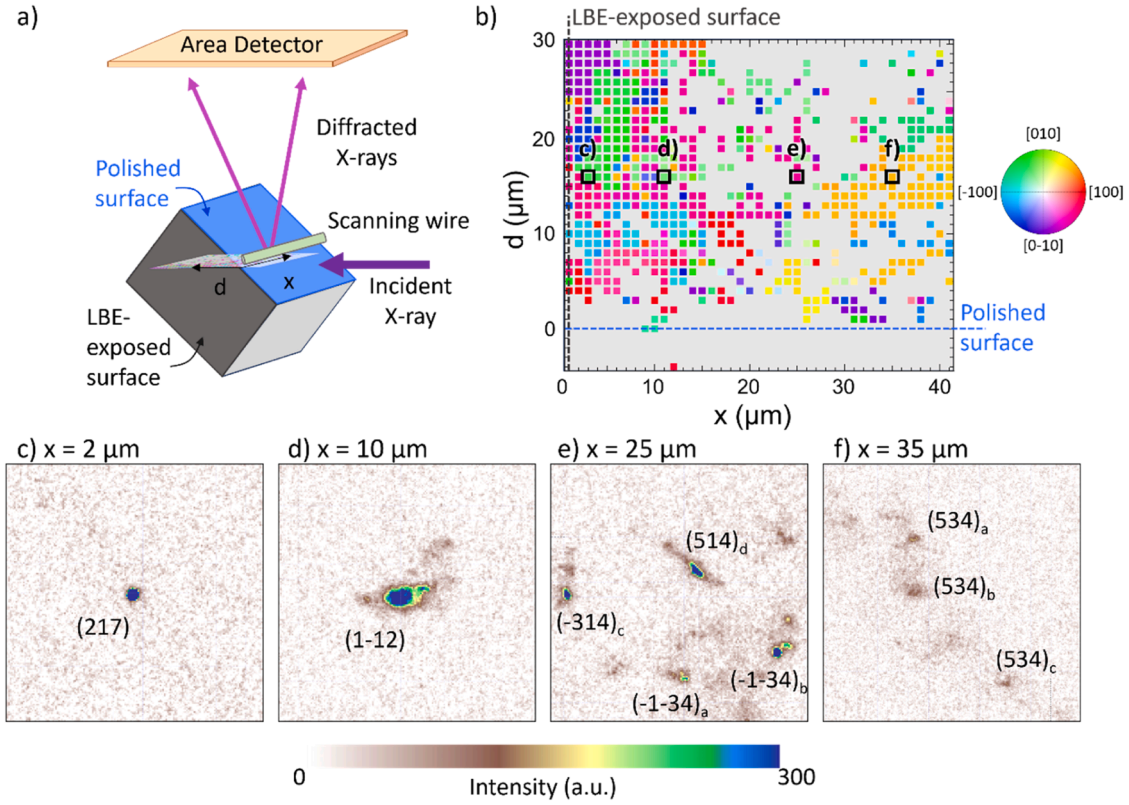

Fig. 3. (a) Schematic of the DAXM measurement setup and coordinates relative to the sample (exposed to LBE corrosion for 70 h at 715 °C) and the LBE-exposed surface (grey). (b) Indexation map (using ferrite crystal structure) measured along the polished surface (x-direction) and at 45° into the sample (d-direction). The LBE-exposed surface lies along x = 0 (grey dashed line) and the polished surface lies along d = 0 (blue dashed line). The pole figure legend is oriented with [001] at its centre along the surface normal of the polished surface. Non-indexed points are shown in white. (c)-(f) Indexed peaks at various depths in the sample. The area of the detector shown in each sub-figure is the same size. Note that for (e) and (f), up to 4 different grains were detected and denoted with subscripts a-d.

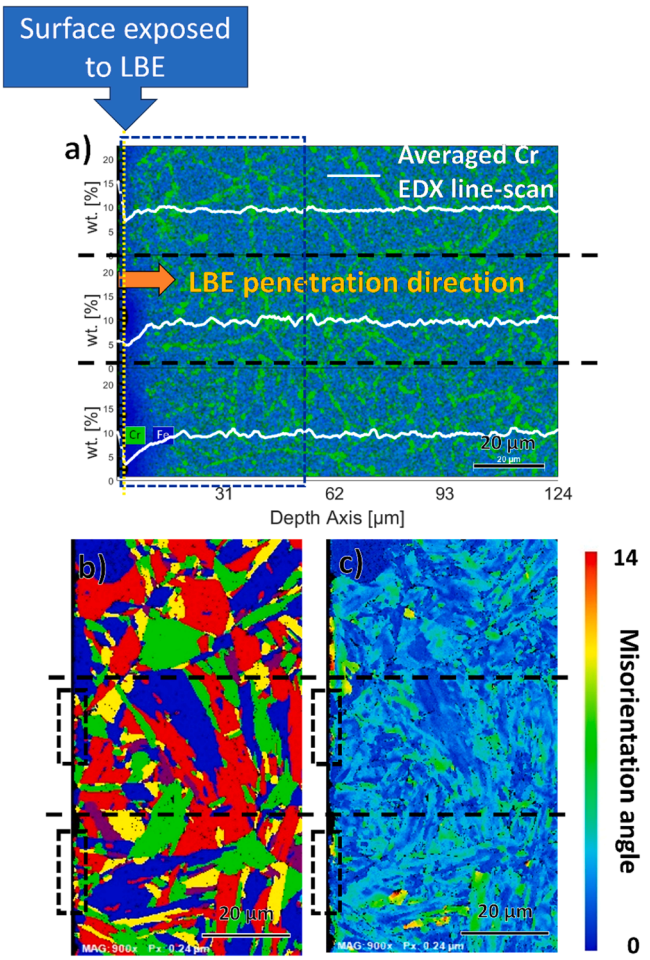

Fig. 4. Cross-section SEM-EBSD and EDX maps for the sample exposed to LBE corrosion for 245 h at 715 °C. (a) EDX map showing Cr and Fe and Cr EDX line-scans in different regions with the LBE penetration direction shown and sample surface marked with a yellow dashed line. The location where Fig. 4(b) and (c) were recorded is marked by the dashed dark blue rectangle. (b) EBSD grain map with small, recrystallized grains highlighted by black dashed rectangles. (c) EBSD grain average misorientation map with scale bar.

region are visible even close to the LBE and T91 interface with some Cr accumulation at the interface which can be attributed to Cr-rich oxides. In comparison, the middle region in this figure exhibits significant levels of Cr depletion and Cr-enriched precipitate dissociation. Finally, the lowest region has most Cr depletion and the greatest reduction of Cr-enriched precipitates. Both the middle and lower regions have no observable Cr accumulation at the LBE-T91 interface. The EBSD grain map and grain average misorientation map in Fig. 4(b) and (c), respectively, show that in comparison to the microstructure before LBE exposure, little change in grain morphology or misorientation can be observed in the upper region. However, the middle and lower regions now incorporate small, recrystallised grains, highlighted by the black dashed rectangle in Fig. 4(b). This suggests the phase transformation occurring at the T91 and LBE interface is a result of Cr depletion, and that the dissociation of Cr precipitates is also influenced by the extent of Cr depletion.

3.4. The Cr carbides dissociation process

To investigate the nature of the Cr precipitates seen in Fig. 1(c), Fig. 2 (d), and Fig. 4(a), and the mechanisms responsible for their dissociation, scanning transmission electron microscopy (STEM) equipped with EELS and EDX detectors was used. Two TEM sample were prepared with one from the LBE and T91 interface here referred to as TEM-1, and the other from the region just beside the interface which is referred to TEM-2. The relative positions of these 2 samples are shown schematically in Fig. 6 (a). Fig. 5(a) shows a STEM image of TEM-2 from the 506 h corroded sample with the different types of precipitates identified. EELS was applied to the region indicated by the red box in Fig. 5(a), with the results shown in Fig. 5(b) - (e). These suggest that the Cr-rich precipitates are Cr carbides. The observed V-rich precipitates contain N, with only a small amount of C, and will be referred to as V nitride. To examine the morphological differences between Cr carbides and V nitrides, a lower magnification STEM image containing several precipitates is shown in Fig. 5(f). Cr carbides have lower contrast and larger size (>100 nm) compared to V nitrides which give higher contrast and are smaller in size (<100 nm). Both Cr carbides and V nitrides are preferentially located at grain boundaries, in agreement with the literature [46,47]. Cr carbides have a round morphology, whereas V nitrides vary from round to disc shaped. Atom probe tomography results that show similar shapes for V nitrides are provided in supplementary figure S3.

Long exposure (~1 hrs) STEM-EDX maps of the sample highlight the significant change in the distribution of Cr, starting at the LBE/T91 interface (sample TEM-1) to deeper locations in the T91 matrix (sample TEM-2). The STEM overview for these two samples are shown in supplementary figure S4. Fig. 6(b) is a zoom-in picture from sample TEM-1 of the corrosion interface and Fig. 6(c) is from sample TEM-2 of the T91 matrix near the interface. Fig. 6(c) shows 2 EDX maps, and the relative positions of maps TEM-1 and TEM-2 are shown in Fig. 6(a). Fig. 6(b) shows there are no Cr carbides close to the LBE. Cr carbides are only seen further from the LBE as shown in Fig. 6(c). A comparison of the 2 EDX maps in Fig. 6(c) suggests a change in the size of Cr carbides, with those closer to the LBE corroded region being larger than those further from the surface. The projected area of Cr carbides highlighted with red boxes in Fig. 6(c) are counted by applying the same threshold to the overall EDX maps. Carbide 1 is 1.47 times larger than carbide 3, and carbide 2 is 1.40 times larger than carbide 3 (see supplementary figure S5 for details). EDX point analysis for the 4 precipitates marked by dashed rectangles in Fig. 6(c) was used to probe any compositional changes. The composition measurements are plotted in Fig. 6(d) and listed in Table 2. In sample TEM-2, the precipitates closer to the LBE interface exhibit higher C content than those further from the surface. From previous studies of carbides in T91, they are expected to be of the form $M_{23}X_6$ (M=Cr, Fe, Mo, or Mn) [48,49]. The Cr: C atomic ratio in the precipitates labelled 3 and 4 is ~ 23:5, whereas precipitates 1 and 2, closer to the corrosion surface, have a much higher C content with an average Cr: C ratio of ~ 23:13. However, we are cautious when interpreting these observations as are they are qualitative and do not represent a quantitative statistical analysis of the distribution of Cr carbides sizes and compositions.

To further investigate the changes in local composition at different distances from the LBE-T91 interface, a systematic set of APT samples, shown in Fig. 7(a), was prepared from the sample exposed to LBE corrosion for 506 h at 715 °C. No Cr carbides were detected in these samples. Thus, the carbon contents detected here suggest the matrix carbon content. The total C content per APT specimen at different depths beneath the surface was measured and is presented in Fig. 7(b). Except for sample 3 in Fig. 7(a), carbon ions were detected at peaks at both 6 Da and 12 Da in the APT mass spectra. Fig. 7(b) provides further confirmation that Cr is deplete near the surface and approaches the bulk concentration when moving deeper into the matrix. Simultaneously, the C content increases towards the surface, displaying a trend opposite to that of Cr. Complementary to the APT analysis, Fig. 7(c) and (d) shows TEM images from sample TEM-1, just beside the LBE and T91 interface, where according to the APT results the C content should be higher and the Cr reduced compared to the matrix. According to the literature, the curved high contrast lines correspond to dislocations, while the dark dots may be interpreted as carbon-enriched phases [50].

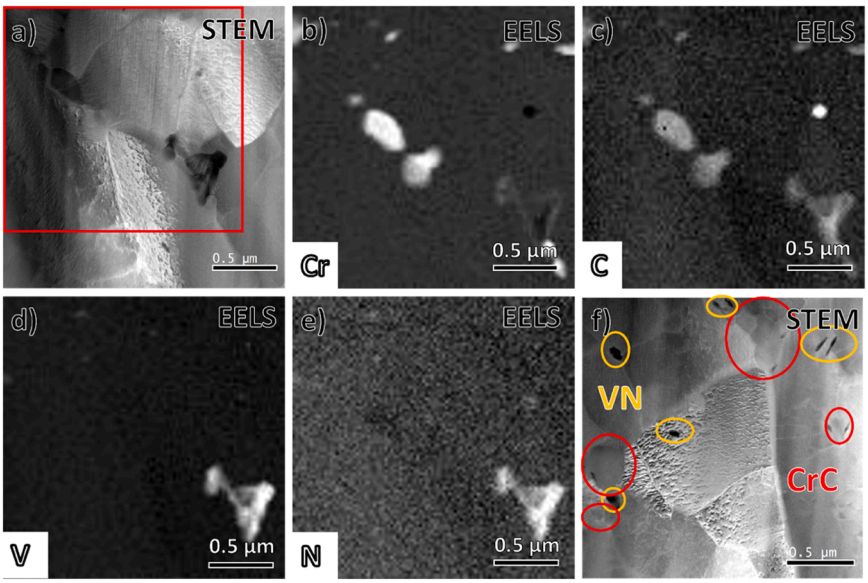

Fig. 5. TEM-2 liftout: (a) STEM image with red box indicating the region for EELS analysis. This region is near the corroded surface of the sample exposed to LBE corrosion for 506 h at 715 °C. Some Cr carbides are still present. (b)-(e) EELS maps corresponding to Cr, C, V, and N, respectively. The area corresponds to the red box shown in (a). (f) STEM image showing Cr carbides (circled in red) and V nitrides (circled in orange).

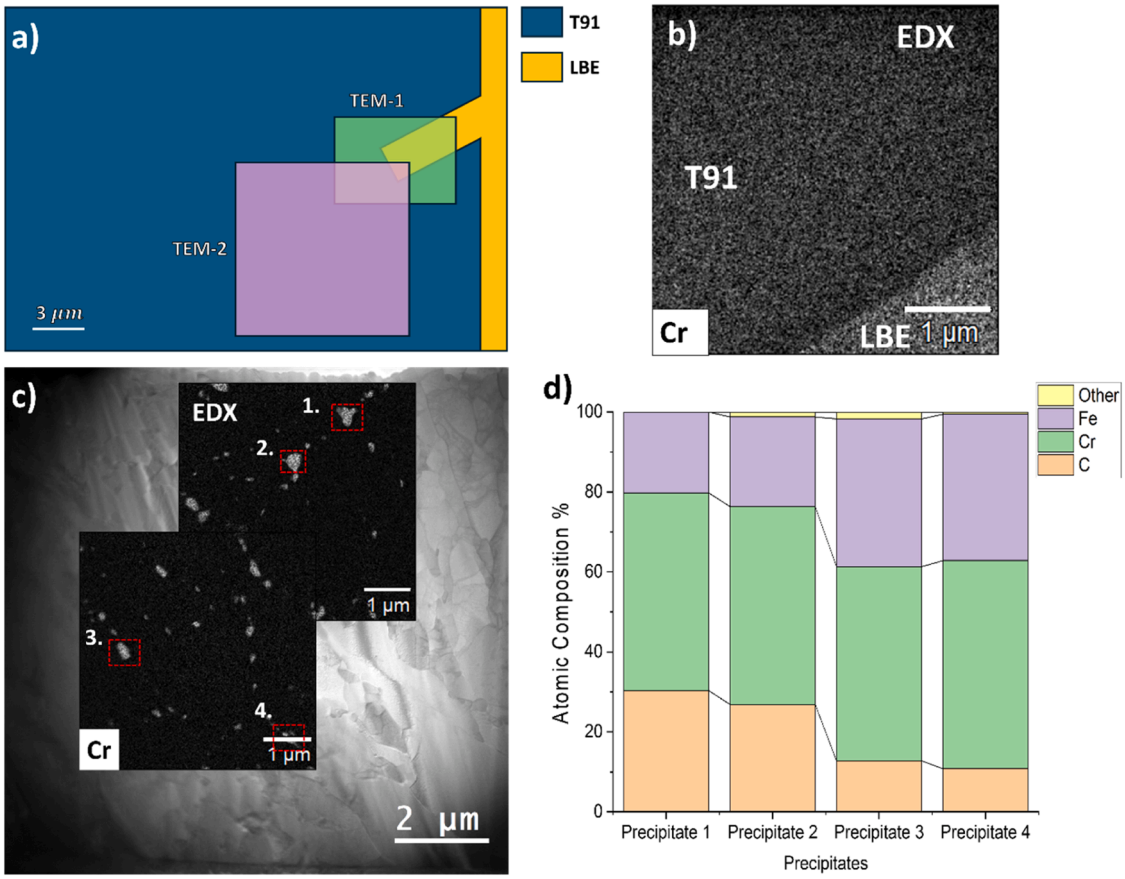

Fig. 6. (a) The relatively position of samples TEM-1 and TEM-2, both extracted from the sample exposed to LBE corrosion for 506 h at 715 °C. (b) STEM-EDX map of Cr from liftout TEM-1 at the T91-LBE interface. There are no Cr precipitates in the matrix adjacent to the LBE. (c) STEM-EDX map of Cr from liftout TEM-2, showing different sizes of Cr precipitates in the matrix at increased distances from the T91-LBE interface. (d) The EDX-derived atomic composition of precipitates 1–4 as highlighted with dashed red rectangles in Fig. 6(c).

Table 2
The atomic composition for precipitates marked in Fig. 6(c).

	C (at%)	Cr (at%)	Fe (at%)
Precipitate 1	30.32	49.43	20.25
Precipitate 2	26.87	49.49	22.42
Precipitate 3	12.77	48.54	36.97
Precipitate 4	10.78	52.06	36.6

4. Discussion

4.1. Phase transformation at the interface of LBE and T91

A clear evolution of grain morphology is seen in Fig. 2(a), which shows equiaxed grains at the interface of T91 and LBE, very distinct from the as-received martensitic T91 material. X-ray diffraction results in Fig. 3(b) further add to this, indexing more readily as ferrite at the corrosion interface in comparison to grains sampled further into the unaffected matrix. Fig. 2(b) and Fig. 2(c), respectively, demonstrate that the new grains have much lower average misorientation and GND density, while Fig. 3(c) indicates that these near-surface grains also have comparatively lower strain. Combined, these results strongly suggest a transformation of martensite grains to ferrite near the interface of T91 and LBE.

4.2. Cr carbides dissociation process

Our results show that LBE corrosion in a reducing environment induces Cr depletion of T91 near the T91-LBE interface. Within the Cr-depleted region, Cr carbides are also dissociated, which can be seen in Fig. 2(d) and Fig. 4(a). We hypothesise the following mechanism for this process: Cr dissolves into the LBE when T91 comes into contact with LBE, as is well documented in the literature [28]. This reduces the Cr content in the matrix surrounding the Cr carbide precipitates. The low Cr content environment destabilises Cr carbides, which start to dissolve. The released Cr also diffuses into the LBE. Due to the low solubility of C in LBE [51], the C lattice concentration in T91 near the LBE interface increases. From the (S)TEM-EDX results shown in Fig. 6, it is proposed that C then diffuses in the opposite direction, away from the surface and deeper into the matrix to form further Cr carbides, increasing the size of existing precipitates. This would promote the formation of a region with a higher number density of Cr carbides or larger precipitates as observed in Fig. 6(c). Considering the relatively low bulk C content in this material (0.09 wt%), the precipitate density and size changing region would be expected to be quite small. Indeed, our results show that this region is only on the order of a few micrometres deep away from the LBE.

Other than the C movement in the opposite direction to Cr, the APT and TEM results in Fig. 7 also suggest an alternative possibility: Some of the C dissociated from Cr carbides may remain in the Cr-depleted region and form other C-enriched phases. Evidence for this is the higher C content at the surface shown in Fig. 7(b) and the apparent C-enriched phases in the TEM images in Fig. 7(c) and (d). There are no carbides detected in this group of APT samples. Thus, the higher C content APT finds in the region corresponds to the bulk concentration. No C-enriched

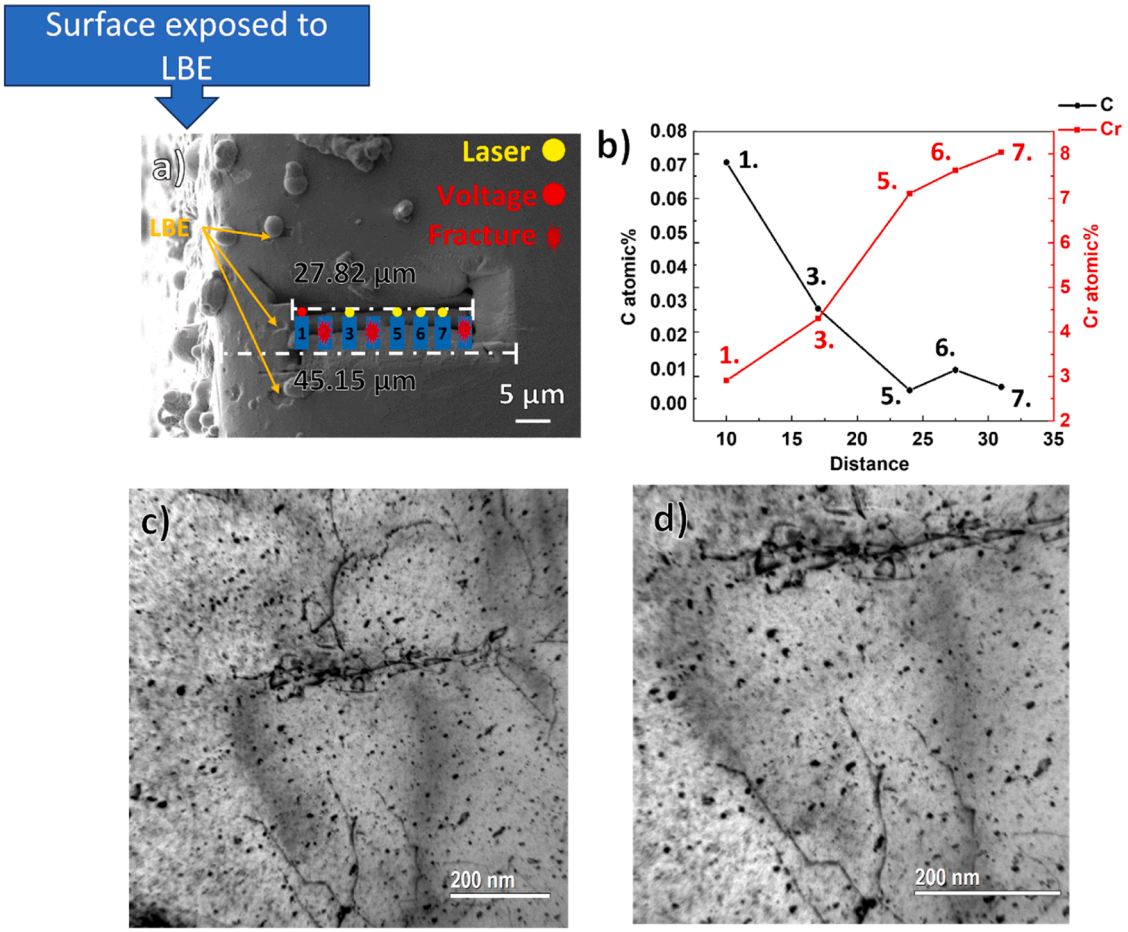

Fig. 7. (a) Indicates regions where APT samples were lifted out from the sample exposed to LBE corrosion for 506 h at 715 °C. LBE is visible on the exposed sample surface. (b) Concentration profile showing the bulk content of C and Cr determined by APT. (c), (d) TEM bright field images from the surface region of TEM-1 experiencing Cr depletion.

phase, as seen in Fig. 7(c) and (d), were seen in the APT reconstructions, perhaps because they are too small to be detected. To summarise, the Cr carbides in the Cr depleted region dissociate with Cr dissolving into LBE and C partially diffusing in the opposite direction to the unaffected T91 matrix and partially remaining within the ferritized grains where it forms other C-enriched phases.

4.3. Correlation between Cr depletion/Cr carbide dissociation and phase transformation

Fig. 2(e) shows that the phase transformation region closely correlates with the region of Cr depletion and Cr carbides dissociation, suggesting these features are related. Fig. 4 supports this hypothesis, by showing that an area at the corrosion surface with no apparent phase transformation also has significantly less Cr depletion and Cr carbide dissociation. Moreover, from Fig. 4, it is apparent that even a relatively small amount of Cr depletion and Cr carbide dissociation will induce small, recrystallised grains. Thus, the following mechanism for the phase transformation can be proposed: Firstly, LBE corrosion results in the Cr depletion at the T91-LBE interface. The lower Cr content leads to a reduced recrystallisation temperature [52,53], meaning that grains with lower Cr content start to recrystallise at the test temperature (715 ℃) while the grains with higher Cr content remain stable. The recrystallisation will initially form small grains, as seen in Fig. 4(b), which then coarsen as shown in Fig. 2(a). Before recrystallisation, there is normally a recovery stage that releases strain in the grains [54]. This may explain our observation of much lower grain average misorientation and GND density in the phase-changed grains as seen in Fig. 2(b), Fig. 2(c) and Fig. 3(c). The recrystallised equiaxed grains are likely to be ferrite rather than martensite which forms either plates or laths [55]. Normally, ferrite has lower C content than martensite, however, the APT results in Fig. 7 show an increased C content in the ferritized region. This can be explained as follows: The highest C content detected in Fig. 7(b) is 0.07 at%, which corresponds to 0.0147 wt%. The solubility of C in ferrite at 723 ℃ is 0.021 wt% according to the Fe-C phase diagram. This is appreciably higher than the highest C content detected. Thus, the C dissociated from Cr carbides and left in this region will not influence the ferritization process. Finally, the upper region of Fig. 4(a), where Cr has accumulated at the LBE and T91 interface, suggests that a continuous Cr oxide scale may act to reduce Cr depletion, which may impede the LBE corrosion of T91.

5. Conclusions

Cr depletion and Cr carbide dissociation has been examined in detail in T91 samples exposed to static LBE corrosion under reducing conditions. Based on EDX and STEM data, we propose the following mechanism:

- The Cr content decreases at the surface of the T91 after contact with LBE.
- The Cr carbides in this region become unstable due to the lower matrix Cr content and undergo dissociation.
- The Cr from dissociated Cr carbides diffuses into the LBE. The released C partially diffuses in the opposite direction, away from the surface, either forming new Cr carbides, or growing existing Cr precipitates in the region not yet depleted of Cr. Some C is also retained near the T91-LBE interface, leading to a higher local C lattice concentration.

A transformation of the microstructure from the original martensitic laths to equiaxed grains with lower defect content is observed up to a similar depth as the Cr depletion. Considering the close correlation between Cr depletion and microstructural transformation, we propose that the Cr depletion is a key driving force for this phase transformation. Based on the experimental evidence, we formulate the following mechanism:

- Cr depletion reduces the recrystallisation temperature for the near-surface grains.
- At the corrosion temperature of 715 ℃ applied in this study, the Cr-depleted grains undergo recovery and recrystallisation from martensite laths to equiaxed ferrite grains, which then continue grow to into larger grains. The recovery stage releases the residual stresses the grains and lattice misorientation is greatly reduced. The retained C from dissociation of Cr carbides will not impede this ferritization process, as the amount of C is below the solubility limit of C in ferrite.

These observations of substantial LBE-induced compositional and morphological changes may have significant consequences for the structural integrity of components exposed to LBE corrosion. Our observations may also guide the design of materials with enhanced LBE corrosion resistance, optimised to mitigate the degradation mechanisms we have identified.

CRediT authorship contribution statement

Scales Robin: Methodology, Data curation. **Zhou Weiyue:** Methodology. **Ding Zhiyuan:** Data curation. **Song Kay:** Methodology, Data curation. **Lapington Mark:** Supervision. **Zhang Minyi:** Writing – review & editing, Writing – original draft, Methodology, Investigation, Formal analysis, Data curation, Conceptualization. **He Guanze:** Formal analysis, Data curation. **Short Michael:** Validation, Supervision, Funding acquisition. **Bagot Paul:** Validation, Supervision. **Moody Michael:** Validation, Supervision, Funding acquisition. **Hofmann Felix:** Validation, Supervision, Funding acquisition.

Declaration of Competing Interest

The authors declare that they have no known competing financial interests or personal relationships that could have appeared to influence the work reported in this paper.

Acknowledgements

EP/T002808/1 Simultaneous Corrosion/Irradiation Testing in Lead and Lead-Bismuth Eutectic: The Radiation Decelerated Corrosion Hypothesis (RC-3). EP/T011505/1 An Atomic-Scale Characterisation Facility for Active Nuclear Materials. NEUP 19–16754Simultaneous Corrosion/Irradiation Testing in Lead and Lead-Bismuth Eutectic: The Radiation Decelerated Corrosion Hypothesis. EP/R010145/1. The authors acknowledge use of characterisation facilities within the David Cockayne Centre for Electron Microscopy, Department of Materials, University of Oxford, alongside financial support provided by the Henry Royce Institute.

Appendix A. Supporting information

Supplementary data associated with this article can be found in the online version at doi:10.1016/j.corsci.2025.112851.

Data availability

Data will be made available on request.

References

[1] B. Grégoire, et al., Corrosion mechanisms of ferritic-martensitic P91 steel and Inconel 600 nickel-based alloy in molten chlorides. Part II: NaCl-KCl-MgCl2 ternary system, Sol. Energy Mater. Sol. Cells 216 (2020) 110675.
[2] G. Yeli, et al., Characterisation of nano-scale precipitates in BOR60 irradiated T91 steel using atom probe tomography, J. Nucl. Mater. (2021) **543**.

[3] J.-B. Vogt, et al., Understanding the liquid metal assisted damage sources in the T91 martensitic steel for safer use of ADS, Eng. Fail. Anal. 14 (6) (2007) 1185–1193.
[4] J. Zhang, N. Li, Review of the studies on fundamental issues in LBE corrosion, J. Nucl. Mater. 373 (1-3) (2008) 351–377.
[5] Chen, Z., K.-C. Chou, and K. Morita, Mechanism of Metastable Wüstite Formation in the Reduction Process of Iron Oxide below 570°C. 2016.
[6] M.P. Popovic, et al., Oxidative passivation of Fe–Cr–Al steels in lead-bismuth eutectic under oxygen-controlled static conditions at 700° and 800° C, J. Nucl. Mater. 523 (2019) 172–181.
[7] K. Lambrinou, et al., Dissolution corrosion of 316L austenitic stainless steels in contact with static liquid lead-bismuth eutectic (LBE) at 500 °C, J. Nucl. Mater. 490 (2017) 9–27.
[8] Weisenburger, A., et al. Stability of oxide layer formed on high-chromium steels in LBE under oxygen content and temperature fluctuation. in The 13th international conference on nuclear engineering abstracts. 2005.
[9] W. Zhou, et al., Proton irradiation-decelerated intergranular corrosion of Ni-Cr alloys in molten salt, Nat. Commun. 11 (1) (2020) 3430.
[10] O. Muránsky, et al., Molten salt corrosion of Ni-Mo-Cr candidate structural materials for Molten Salt Reactor (MSR) systems, Corros. Sci. 159 (2019) 108087.
[11] C. Schroer, et al., Selective leaching of nickel and chromium from Type 316 austenitic steel in oxygen-containing lead–bismuth eutectic (LBE), Corros. Sci. 84 (2014) 113–124.
[12] Klok, O., Liquid Metal Corrosion Effects in MYRRHA candidate 316L Austenitic Stainless Steel. Vrije Universiteit Brussel, 2018.
[13] P. Hosemann, et al., Twin boundary-accelerated ferritization of austenitic stainless steels in liquid lead–bismuth eutectic, Scr. Mater. 118 (2016) 37–40.
[14] Y. Kurata, M. Futakawa, S. Saito, Comparison of the corrosion behavior of austenitic and ferritic/martensitic steels exposed to static liquid Pb–Bi at 450 and 550°C, J. Nucl. Mater. 343 (1-3) (2005) 333–340.
[15] L. Medina-Almazán, T. Auger, D. Gorse, Liquid metal embrittlement of an austenitic 316L type and a ferritic–martensitic T91 type steel by mercury, J. Nucl. Mater. 376 (3) (2008) 312–316.
[16] A. Weisenburger, et al., Creep, creep-rupture tests of Al-surface-alloyed T91 steel in liquid lead bismuth at 500 and 550C, J. Nucl. Mater. 431 (1-3) (2012) 77–84.
[17] D. Gorse, et al., Influence of liquid lead and lead–bismuth eutectic on tensile, fatigue and creep properties of ferritic/martensitic and austenitic steels for transmutation systems, J. Nucl. Mater. 415 (3) (2011) 284–292.
[18] M. Zhang, et al., Nano-scale corrosion mechanism of T91 steel in static lead-bismuth eutectic: a combined APT, EBSD, and STEM investigation, Acta Mater. (2024) 119883.
[19] Y. Li, et al., Mechanical properties and phases evolution in T91 steel during long-term high-temperature exposure, Eng. Fail. Anal. 111 (2020) 104451.
[20] J. Liu, et al., Lead–bismuth eutectic corrosion behaviors of ferritic/martensitic steels in low oxygen concentration environment, Oxid. Met. 84 (2015) 383–395.
[21] G.S. Was, T.R. Allen, Corrosion issues in current and next-generation nuclear reactors, Struct. Alloy. Nucl. Energy Appl. (2019) 211–246.
[22] C. Cabet, F. Rouillard, Corrosion issues of high temperature reactor structural metallic materials, J. Eng. Gas. Turbines Power 131 (2009) 6.
[23] G.S. Was, et al., Materials for future nuclear energy systems, J. Nucl. Mater. 527 (2019) 151837.
[24] R.N. Durham, B. Gleeson, D.J. Young, Factors affecting chromium carbide precipitate dissolution during alloy oxidation, Oxid. Met. 50 (1998) 139–165.
[25] Q. Liao, et al., Investigation into creep-to-rupture of SIMP steel in stagnant LBE at 300–450°C. Materials and Corrosion 73 (5) (2022) 784–797.
[26] C. Schroer, et al., Silicon-containing ferritic/martensitic steel after exposure to oxygen-containing flowing lead–bismuth eutectic at 450 and 550 °C, J. Nucl. Mater. 469 (2016) 162–176.
[27] Guntz, G., et al., The T91 book. Vallourec Industries, 1990.
[28] M.P. Short, R.G. Ballinger, H.E. Hänninen, Corrosion resistance of alloys F91 and Fe–12Cr–2Si in lead–bismuth eutectic up to 715C, J. Nucl. Mater. 434 (1-3) (2013) 259–281.
[29] M.T. Lapington, et al., Characterisation of corrosion damage in T91/F91 steel exposed to static liquid lead-bismuth eutectic at 700-715° C, J. Nucl. Mater. (2023) 154687.
[30] Fazio, C., et al., Handbook on lead-bismuth eutectic alloy and lead properties, materials compatibility, thermal-hydraulics and technologies-2015 edition. 2015, Organisation for Economic Co-Operation and Development.
[31] Zhang, M., et al., Nano-Scale Corrosion Mechanism of T91 Steel in Static Lead-Bismuth Eutectic: A Combined Apt, Ebsd, and Stem Investigation. SSRN, 2023.
[32] M. Meisnar, et al., Low-energy EDX–A novel approach to study stress corrosion cracking in SUS304 stainless steel via scanning electron microscopy, Micron 66 (2014) 16–22.
[33] T.B. Britton, A.J. Wilkinson, Measurement of residual elastic strain and lattice rotations with high resolution electron backscatter diffraction, Ultramicroscopy 111 (8) (2011) 1395–1404.
[34] Wilkinson, A.J., et al. A review of advances and challenges in EBSD strain mapping. in IOP Conference Series: Materials Science and Engineering. 2014. IOP Publishing.
[35] B.C. Larson, et al., Three-dimensional X-ray structural microscopy with submicrometre resolution, Nature 415 (6874) (2002) 887–890.
[36] W. Liu, et al., The three-dimensional X-ray crystal microscope: a new tool for materials characterization, Metall. Mater. Trans. A 35 (2004) 1963–1967.
[37] S. Lozano-Perez, A guide on FIB preparation of samples containing stress corrosion crack tips for TEM and atom-probe analysis, Micron 39 (3) (2008) 320–328.
[38] W.E. Berry, C.V. King, Corrosion in nuclear applications, J. Electrochem. Soc. 118 (12) (1971) 311C.
[39] E. Charalampopoulou, et al., Orientation relationship of the austenite-to-ferrite transformation in austenitic stainless steels due to dissolution corrosion in contact with liquid Pb-Bi eutectic, Scr. Mater. 167 (2019) 66–70.
[40] Nowell, M.M., S.I. Wright, and J.O. Carpenter, Differentiating ferrite and martensite in steel microstructures using electron backscatter diffraction. Proceedings of the Materials Science and Technology (MS&T), Pittsburgh, PA, USA, 2009: p. 25-29.
[41] Rl Barabash, et al., White microbeam diffraction from distorted crystals, Appl. Phys. Lett. 79 (6) (2001) 749–751.
[42] R.I. Barabash, et al., Quantitative analysis of dislocation arrangements induced by electromigration in a passivated Al (0.5 wt% Cu) interconnect, J. Appl. Phys. 93 (9) (2003) 5701–5706.
[43] R.I. Barabash, et al., Polychromatic microdiffraction characterization of defect gradients in severely deformed materials, Micron 40 (1) (2009) 28–36.
[44] F. Hofmann, S. Keegan, A.M. Korsunsky, Diffraction post-processing of 3D dislocation dynamics simulations for direct comparison with micro-beam Laue experiments, Mater. Lett. 89 (2012) 66–69.
[45] X. Chen, et al., Quantitative microstructural imaging by scanning Laue x-ray micro- and nanodiffraction, MRS Bull. 41 (6) (2016) 445–453.
[46] N. Saini, et al., A comparative study of ductile-brittle transition behavior and fractography of P91 and P92 steel, Eng. Fail. Anal. 81 (2017) 245–253.
[47] K. Guguloth, N. Roy, Study on the creep deformation behavior and characterization of 9Cr-1Mo-V-Nb steel at elevated temperatures, Mater. Charact. 146 (2018) 279–298.
[48] F. Abe, Precipitate design for creep strengthening of 9% Cr tempered martensitic steel for ultra-supercritical power plants, Sci. Technol. Adv. Mater. 9 (1) (2008) 013002.
[49] A. Zeman, et al., Microstructural analysis of candidate steels pre-selected for new advanced reactor systems, J. Nucl. Mater. 362 (2-3) (2007) 259–267.
[50] Challa, V.S.A., et al., The Effect of Coiling Temperature on the Mechanical Properties of Ultrahigh-Strength 700 MPa Grade Processed via Thin-Slab Casting. Proceedings of the AISTech, 2014: p. 2987-2997.
[51] C.B. Griffith, M.W. Mallett, The solubility of carbon and oxygen in liquid bismuth, J. Am. Chem. Soc. 75 (8) (1953) 1832–1834.
[52] S. YAMAMOTO, T. SAKIYAMA, C. OUCHI, Effect of alloying elements on recrystallization kinetics after hot deformation in austenitic stainless steels, Trans. Iron Steel Inst. Jpn. 27 (6) (1987) 446–452.
[53] L. Ma, et al., Effects of Cr content on the microstructure and properties of 26Cr–3.5 Mo–2Ni and 29Cr–3.5 Mo–2Ni super ferritic stainless steels, J. Mater. Sci. Technol. 32 (6) (2016) 552–560.
[54] C.M.D. Moorthy, J.N. Reddy, Recovery of interlaminar stresses and strain energy release rates in composite laminates, Finite Elem. Anal. Des. 33 (1) (1999) 1–27.
[55] G. Krauss, Steels: processing, structure, and performance, Asm International, 2015.